# Improved FRF Acquisition Method for Vehicle Body NVH Analysis

**Tom Knechten** and **Peter J. G. van der Linden**, Siemens PLM software, Leuven, Belgium

**Marius-Cristian Morariu**, Morariu Consultancy Ltd., Warwickshire, United Kingdom

Structural and vibroacoustic transfer functions still form an essential part of NVH data in vehicle development programs. Excitation in three DOFs at all body interface connection locations to target responses gives information on local dynamics stiffness and body sensitivity for a specific path in an efficient manner. However, vehicles have become more compact for fuel efficiency, production costs and to meet the market demand for urban vehicles. Alternative driveline concepts increase the electronic content and new mount locations. Here we propose a method that enables the engineer to obtain all relevant FRFs in and around the body structure. The method is based on multiple excitations in a locally rotated coordinate system that are recombined to obtain the desired FRFs in three global directions. This way the engineer is able to select excitation orientations that are accessible.

Structural and vibro-acoustic transfer functions still form an essential part of NVH data in vehicle development programs.[1] Excitation in three orthogonal DOFs (degrees of freedom) at body interface connections to target responses gives information on local dynamic stiffness and body sensitivities for that specific path. These target responses can be occupant ear locations or steering wheel vibrations for example. Structural responses measured near the force input location gives information on local dynamics. Several trends make the current practices in obtaining this data in an accurate and efficient way more challenging. So a new method has been developed and will be discussed in this article.

Vehicles become more compact to meet fuel efficiency and production cost targets and to meet the market demand for urban vehicles.[2] Alternative driveline concepts increase the electronic content[3] and add new mount locations, as shown in Figure 1.[4] To achieve the optimum on-road noise NVH, handling performance while conserving interior space and trunk volume require complex suspension layouts. On top of that, customers emphasis on safety and comfort systems results in a higher packaging density.[3] The trend of shorter vehicle model lifetime puts pressure on development time. Platform sharing offers the auto OEMs a reduction in engineering effort as the hard points are fixed for a product family.[5] But another trend, namely the increase of the number of product variants,[5] increases the need for efficient testing methods as the NVH performance is determined by the total body, not only by its platform.

Increased space constraints and increasing number of mount locations make it a more time-consuming job for the test engineer to obtain accurate results efficiently using current practices.[6] There are different ways to obtain NVH information about the trimmed body. Reciprocal methods for vibroacoustic transfer function testing have been applied successfully many times,[7] but they do not give any additional local structural information like local dynamic stiffness of an interface location. Direct excitation methods do give the possibility to obtain local structural information.

Traditional modal hammer excitations intended for component testing will requires trained and experienced engineers, making it a tedious job.[8] Traditional modal shaker excitation requires a long installation time and cannot be applied in many locations and orientations due to the necessity of external supports. Self-suspending and self-aligning inertia shakers are rather new tools for vehicle testing.

An inertial shaker is directly attached at the excitation location, and as long as the dynamic mass loading in off-axial directions are kept low, the measurements are accurate and repeatable.[9] Inertial
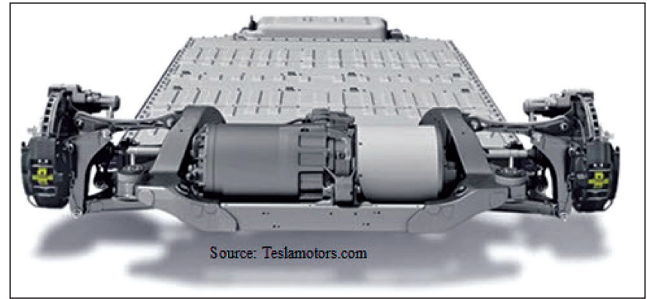
Figure 1. New driveline concepts make structural testing challenging in terms of accessibility, number of mounts, and packaging density.

shaker size is relatively small and can be attached in any orientation. But there are main vehicle axes that cannot be accessed. In this article, a method is proposed to enable the engineer to obtain all relevant FRFs in and around the body structure by removing the space constraint associated with inertial shakers. Instead of a fixed relation between the excitation direction and the space the shaker occupies, the operator can select the space the shaker envelope needs. With the proposed method, the operator can select in which angles the excitation is done, and by geometric processing the measured data can be oriented in the global vehicle axis system or local mount plane.

The first section describes the analytical model consisting of geometric conversion using pseudo-matrix inversions. The experimental validation section describes an application case on a trimmed body. In this section, the test sequence is described and the results are compared with reciprocal data as validation of the method. The conclusions will highlight the current possibilities and future potential improvements.

## Theoretical Approach

**FRF Reconstruction Using Euler Angles**. A 3D adapter is hardware between the test object and inertial shaker that enables selective positioning and is designed to permit excitation at fixed angles. The Euler angles $\beta$ and $\alpha$ are used to define the orientation of excitation relative to the vehicle coordinate axis. $\alpha$ is the angle between the direction of excitation and X direction in the XY plane, and $\beta$ is the angle between the direction of excitation and the horizontal XY plane, as shown in Figure 2.

The transfer functions $H_i$ from the adapter to the response need to be measured by exciting with a force $F_i$ in the possible directions and measuring the response accelerations $X_i$. At least 3 directions need to be used to recompose the three FRFs in orthogonal directions X, Y and Z.

$$\begin{cases} F_1 \cdot H_1 = X_1 \\ F_2 \cdot H_2 = X_2 \\ \quad \vdots \\ F_i \cdot H_i = X_i \end{cases} \tag{1}$$

Each equation from the previous system can be written as a sum of products between orthogonal-oriented forces and the desired transfer functions:

$$\begin{cases} F_{1x} \cdot H_x + F_{1y} \cdot H_y + F_{1z} \cdot H_z = X_1 \\ F_{2x} \cdot H_x + F_{2y} \cdot H_y + F_{2z} \cdot H_z = X_2 \\ \quad \vdots \\ F_{ix} \cdot H_x + F_{iy} \cdot H_y + F_{iz} \cdot H_z = X_i \end{cases} \tag{2}$$

where, each orthogonal force component can be written:

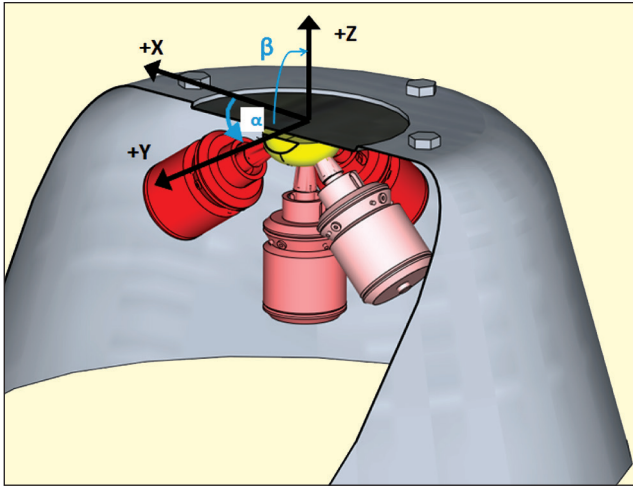Figure 2. Graphic representation of Euler angles and relative to vehicle axes X, Y and Z depicted on top of front shock tower body connection.



Figure 3. Trimmed vehicle body suspended on bungee ropes in semi-anechoic chamber.

$$F_x = F \cdot \cos\beta \cdot \cos\alpha$$
$$F_y = F \cdot \cos\beta \cdot \sin\alpha \qquad (3)$$
$$F_z = F \cdot \sin\beta$$

By integrating Equation 3 in equation 2 and equalizing the results with Equation 1, we obtain:

$$\begin{cases} F_1 \cos\beta_1 \cdot \cos\alpha_1 \cdot H_x + F_1 \cdot \cos\beta_1 \cdot \sin\alpha_1 \cdot H_y + F_1 \sin\beta_1 \cdot H_z = F_1 \cdot H_1 \\ F_2 \cos\beta_2 \cdot \cos\alpha_2 \cdot H_x + F_2 \cdot \cos\beta_2 \cdot \sin\alpha_2 \cdot H_y + F_2 \sin\beta_2 \cdot H_z = F_2 \cdot H_2 \\ \vdots \\ F_i \cos\beta_i \cdot \cos\alpha_i \cdot H_x + F_i \cdot \cos\beta_i \cdot \sin\alpha_i \cdot H_y + F_i \sin\beta_i \cdot H_z = F_i \cdot H_i \end{cases} \qquad (4)$$

The system can be written in a matrix form as follows:

$$\begin{bmatrix} \cos\beta_1 \cdot \cos\alpha_1 & \cos\beta_1 \cdot \sin\alpha_1 & \sin\beta_1 \\ \vdots & \vdots & \vdots \\ \cos\beta_i \cdot \cos\alpha_i & \cos\beta_i \cdot \sin\alpha_i & \sin\beta_i \end{bmatrix} \cdot \begin{bmatrix} H_x \\ H_y \\ H_z \end{bmatrix} = \begin{bmatrix} H_1 \\ H_2 \\ \vdots \\ H_z \end{bmatrix} \qquad (5)$$

Equation 5 can be represented symbolically as:

$$A \cdot FRF = H \qquad (6)$$

The remaining task is to calculate the desired FRF matrix by multiplying the inverse matrix $A^{-1}$ with the measured transfer matrix $H$:

$$FRF = A^{-1} \cdot H \qquad (7)$$

In case matrix $A$ is a rectangular matrix of $m \times n$ elements, the pseudo-inverse is calculated by using the singular-value decomposition method.

**Pseudo-Matrix Inversion Using Singular Value Decomposition (SVD).** The singular-value decomposition is a powerful tool to reveal the numerical problems that the ill-conditioned matrix A creates. A general SVD is applied to the rectangular FRF matrix $A \in R^{m \times n}$, with $m > n$.[11]

The matrix $A$ is decomposed as:

$$A = U\Sigma V^T = \sum_{i=1}^{n} u_i \sigma_i v_i^T \qquad (8)$$

where $U = (u_i, ..., u_n)$ and $V = v_i, ... , v_n$ are matrices with orthonormal columns. This means that $U^T U = I$ and $V^T V = I$. The elements of $u_i, v_i$ are column vectors with $u_i$ having $m$ elements and $v_i$ having $n$ elements. The matrix $\Sigma$ is a diagonal matrix with non-negative components arranged in a decreasing order:

$$\Sigma = \begin{pmatrix} \sigma_i & 0 & \cdots & 0 \\ 0 & \sigma_2 & \cdots & 0 \\ \vdots & \vdots & \ddots & \vdots \\ 0 & 0 & \cdots & \sigma_n \end{pmatrix} \qquad (9)$$

where $\sigma_1 \geq \sigma_2 \geq ... \geq \sigma_n \geq 0$ are the singular values of the matrix $A$.

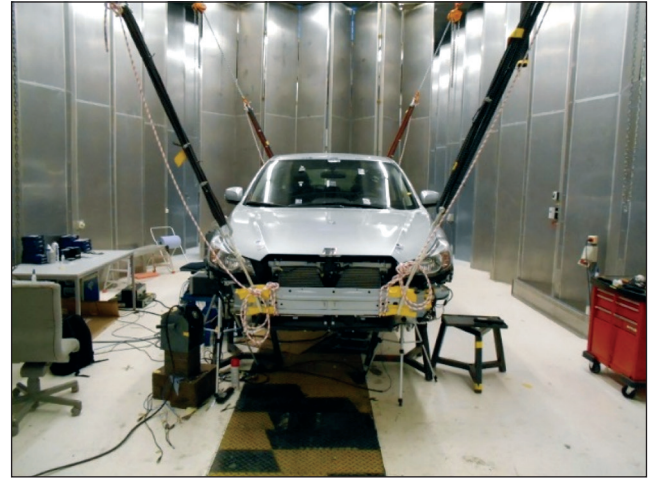The truncated SVD is applied to calculate the pseudo-inverse of the matrix $A$. The pseudo inverse of a matrix is known also by the name of Moore-Penrose pseudo inverse and is noted with $A^+$.[11] The common use of the pseudo inverse is to compute a best-fit (least-squares) solution of a system of a linear equation that doesn't have a unique solution.

The most common way to calculate the pseudo inverse is by using the SVD technique:

$$A^+ = V\Sigma^+ U^H \qquad (10)$$

where $\Sigma^+ = \text{diag}(\sigma_1^{-1}, \sigma_2^{-1}, \sigma_3^{-1}, ... , \sigma_n^{-1}$ if there are not singular values equal with zero, and $\sigma+ = \text{diag}(\sigma_1^{-1}, \sigma_2^{-1}, \sigma_3^{-1}, ... , \sigma_n^{-1}$ if the last $n - q$ singular values are truncated.

## Experimental Validation of Method

To verify the theory, a practical case was chosen. A vehicle-trimmed body was suspended on bungee cords (see Figure 3), simulating a free-free condition. The vibration frequency response functions (FRFs) were measured between the connection points of the suspension, engine and steering rack, exactly as it would be done for a NVH troubleshooting case, like TPA (transfer path analysis), for example. The structure-borne road noise is relevant in the low-mid frequency range,[8,9] but the analysis range was extended up to 2 kHz for observation.

Some structures that required more attention were the suspension domes because of two reasons. First, they are low-stiffness connection points of the suspension, which makes them sensitive to mass loading. Two, they are almost impossible to access accurately with current practices. The space is just too narrow to permit hammer excitation. Another option was to measure the reciprocal FRFs, but the driving-point information was not available for that specific location.

**Setup**. An inertial LMS Qsources shaker was used to excite the body on the noted locations. At the points where the excitation was not possible in all the three orthogonal directions of the vehicle coordinate axis, a light aluminum block was added between the structure and the shaker. Figure 4 shows the attachment setup at the location of the front-right top strut mount.

An aluminum block is a practical solution to be able to excite close to the connection in the desired direction. Several risks exist within this solution: the added element can cause additional local dynamics not belonging to the vehicle body, and the shifted position might not be equivalent for the connection interface anymore. The impact on the FRF of these errors increases with increasing frequency and depends on the local body structural properties.

The proposed solution here uses a 3D adapter like the one displayed in Figure 5. This device assures that the force is applied in the desired point while eliminating the unwanted moment effect. The stinger, which has the role to support the shaker and transmit the force, fits into several threaded holes distributed radially from the center of the adapter. The user has the option to choose different excitation directions, which form fixed angles with the attachment surface.
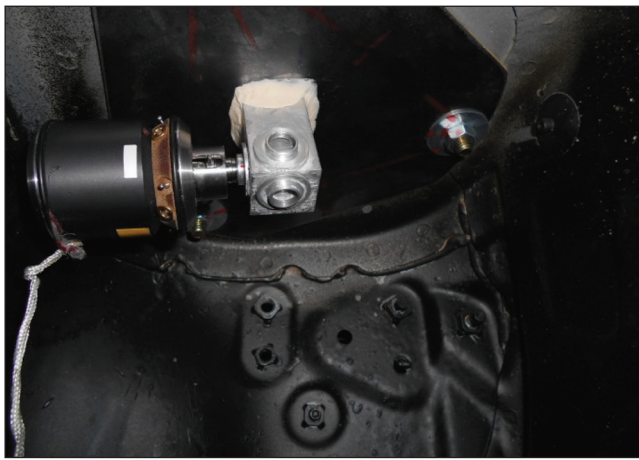
Figure 4. LMS Qsources inertia shaker fixed to an aluminum block at top strut mount.



Figure 5. LMS Qsources integral shaker with 3D adapter at front top strut mount location.

In this way, knowing the angles between excitation and vehicle's main axis, the user can calculate the FRFs in the vehicle coordinate system from a minimum of three FRFs when excitations are performed in oblique directions.

The response accelerations were measured at every input location to check the reciprocity. The adapter contains a built in 3D accelerometer that permits measuring the local FRFs.

**Global View of Vehicle FRFs.** The FRFs were measured on the right side of the vehicle at front and rear suspension connection points. Both direct and reciprocal FRFs were selected to check the reciprocity of the functions and validate the measurements. Because of the large amount of functions to be compared, the frequency response assurance criterion (FRAC) was used to observe their global tendency in a frequency assurance criterion matrix. This criterion has values from 0 to 1; a number closer to 1 representing a good reciprocity, while closer to 0 meaning big shifts in resonance frequency or differences in amplitude of the FRFs. According to the definition, it has the following formula:[10]

$$ FRAC = \frac{\left| H_i * H_j^H \right|^2}{\left| H_i * H_i^H \right| \left\| H_j * H_j^H \right\|} \quad (11) $$

where $H_i$ is the direct FRF, $H_i$ is the inverse FRF, $H_i^H$ is the transpose of the direct FRF and $H_j^H$ is the transpose of the inverse FRF.

The resulting FRAC matrix showed good reciprocity between the FRFs in both the cases from 30 Hz up to a frequency of 300 Hz. Figure 6 represents measured data extracts from the global FRAC matrix containing the values of the direct and reciprocal FRFs between two excitation points, namely, the top strut mount

|  | FDOM | FDOM | FDOM | FRAR | FRAR | FRAR |
|---|---|---|---|---|---|---|
|  | FRRI:X | FRRI:Y | FRRI:Z | FRON:X | FRON:Y | FRON:Z |
| FDOM:FRRI:X | 1.00 | 0.99 | 0.81 | 0.99 | 0.95 | 0.81 |
| FDOM:FRRI:Y | 0.99 | 1.00 | 0.80 | 0.95 | 0.96 | 0.98 |
| FDOM:FRRI:Z | 0.81 | 0.80 | 1.00 | 0.96 | 0.96 | 1.00 |
| FRAR:FRON:X | 0.99 | 0.95 | 0.96 | 1.00 | 0.99 | 0.95 |
| FRAR:FRON:Y | 0.95 | 0.96 | 0.96 | 0.99 | 1.00 | 0.98 |
| FRAR:FRON:Z | 0.81 | 0.98 | 1.00 | 0.95 | 0.98 | 1.00 |

Figure 6. Extract from FRAC matrices of direct and reciprocal from 30 to 300 Hz (measured FRFs).

|  | FDOM | FDOM | FDOM | FRAR | FRAR | FRAR |
|---|---|---|---|---|---|---|
|  | FRRI:X | FRRI:Y | FRRI:Z | FRON:X | FRON:Y | FRON:Z |
| FDOM:FRRI:X | 1.00 | 0.99 | 0.99 | 0.99 | 0.98 | 0.99 |
| FDOM:FRRI:Y | 0.99 | 1.00 | 0.89 | 0.96 | 0.97 | 0.99 |
| FDOM:FRRI:Z | 0.99 | 0.89 | 1.00 | 0.95 | 0.95 | 1.00 |
| FRAR:FRON:X | 0.99 | 0.96 | 0.95 | 1.00 | 0.99 | 0.98 |
| FRAR:FRON:Y | 0.98 | 0.97 | 0.95 | 0.99 | 1.00 | 0.93 |
| FRAR:FRON:Z | 0.99 | 0.99 | 1.00 | 0.98 | 0.93 | 1.00 |

Figure 7. Extract from FRAC matrices of direct and reciprocal FRFs from 30 to 300 Hz (reconstructed FRFs).

|  | FDOM | FDOM | FDOM | FRAR | FRAR | FRAR |
|---|---|---|---|---|---|---|
|  | FRRI:X | FRRI:Y | FRRI:Z | FRON:X | FRON:Y | FRON:Z |
| FDOM:FRRI:X | 1.00 | 0.04 | 0.58 | 0.49 | 0.50 | 0.29 |
| FDOM:FRRI:Y | 1.04 | 1.00 | 0.60 | 0.63 | 0.37 | 0.36 |
| FDOM:FRRI:Z | 0.58 | 0.60 | 1.00 | 0.32 | 0.43 | 0.37 |
| FRAR:FRON:X | 0.49 | 0.63 | 0.32 | 1.00 | 0.99 | 1.00 |
| FRAR:FRON:Y | 0.50 | 0.37 | 0.43 | 0.99 | 1.00 | 0.99 |
| FRAR:FRON:Z | 0.29 | 0.36 | 0.37 | 1.00 | 0.99 | 1.00 |

Figure 8. Extract from FRAC matrices of direct and reciprocal FRFs from 300 to 600 Hz (measured FRFs).

|  | FDOM | FDOM | FDOM | FRAR | FRAR | FRAR |
|---|---|---|---|---|---|---|
|  | FRRI:X | FRRI:Y | FRRI:Z | FRON:X | FRON:Y | FRON:Z |
| FDOM:FRRI:X | 1.00 | 0.23 | 0.44 | 0.86 | 0.88 | 0.52 |
| FDOM:FRRI:Y | 0.23 | 1.00 | 0.54 | 0.71 | 0.44 | 0.45 |
| FDOM:FRRI:Z | 0.44 | 0.54 | 1.00 | 0.31 | 0.26 | 0.44 |
| FRAR:FRON:X | 0.86 | 0.71 | 0.31 | 1.00 | 0.95 | 0.84 |
| FRAR:FRON:Y | 0.88 | 0.44 | 0.26 | 0.95 | 1.00 | 0.96 |
| FRAR:FRON:Z | 0.52 | 0.45 | 0.44 | 0.84 | 0.96 | 1.00 |

Figure 9. Extract from FRAC matrices of direct and reciprocal FRFs from 300 to 600 Hz (reconstructed FRFs).

connection noted with FDOM:FRRI and the front arm front connection, noted with FRAR:FRON. Figure 7 shows the same matrix for the reconstructed FRFs. Note that the local FRFs at the front dome in Z direction were significantly improved.

The FRAC matrices were also calculated for the frequency ranges between 300 and 600 Hz. In the case where the excitation was performed from high stiffness points, the reciprocity was good for both the methods. Figure 8 shows the matrix for measured data, while Figure 9 depicts the matrix for the reconstructed FRFs. For the case where the FRFs were measured in the vehicle orthogonal directions, the reciprocity of the cross-vehicle measurements was not valid anymore, which showed the limitations of the initial excitation method. For the case in which the orthogonal FRFs were recomposed from oblique excitation transfer functions, the reciprocity showed some improvements especially in the Z direction, but it was still not good (see Figure 9).

The proposed method proved to successfully replace the classic excitation method up to 300 Hz and showed improvements in the higher frequency range at the low-stiffness locations. To further understand the phenomena, some FRF plots were analyzed in detail in the following subsection.
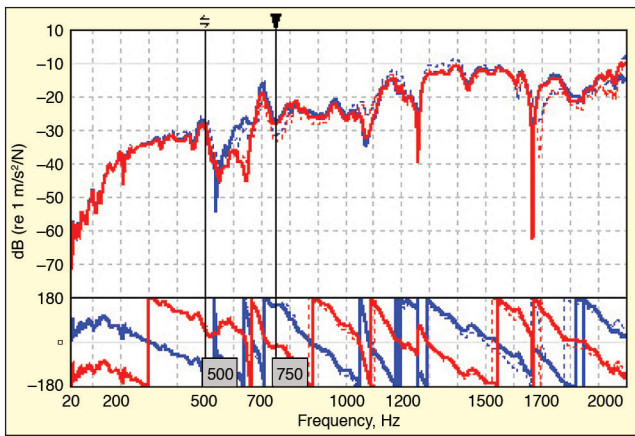
*Figure 10. Direct and reciprocal FRFs between right front arm's connections: red bold line – direct FRF measured; red dotted line – reciprocal FRF measured; blue bold line – direct FRF calculated; blue dotted line – reciprocal FRF calculated.*
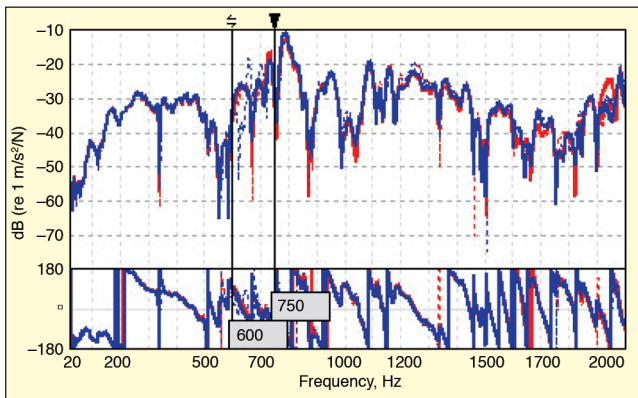


*Figure 11. Direct and reciprocal FRFs between right front and rear arms connections: red bold line – direct FRF measured; red dotted line – reciprocal FRF measured; blue bold line – direct FRF calculated; blue dotted line – reciprocal FRF calculated.*
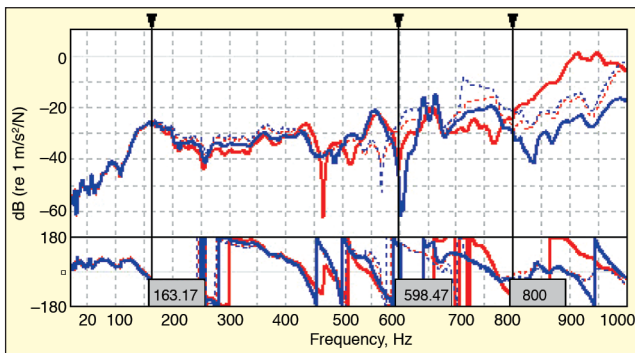


*Figure 12. Direct and reciprocal FRFs between right front arm and top strut mount connections: red bold line – direct FRF measured; red dotted line – reciprocal FRF measured; blue bold line – direct FRF calculated; blue dotted line – reciprocal FRF calculated.*

**FRF Reciprocity Analyzed for Particular Locations**. Some local and cross-vehicle FRFs were analyzed for reciprocity on a frequency range from 30 to 2000 Hz. The cross-vehicle FRFs are important to check if the excitation in oblique directions are accurate enough for a good reconstruction of FRFs between local and distant points in the vehicle axis of coordinates.

### FRFs Between Front-Arm Connection Points

The reciprocity of the FRFs was checked between the right front arm's connections: FRAR:FRON and FRAR:REAR in the Z direction. The plots of the FRFs are displayed in Figure 10.The reciprocity of the measured FRFs was good over the studied frequency range. The calculated direct and reciprocal FRFs match the measured ones with an exception between 500 and 750 Hz. In Table 1, the FRAC results are displayed for the two cases.

### FRFs between Right Front and Rear Arms

The reciprocity of the FRFs was checked between the front-right arm's front connection and rear subframe front connection: FRAR:FRRI and RSUB:FRRI. The reciprocity of the measured FRFs was again good over the whole frequency range. The calculated reciprocal FRF was good up to 600 Hz, then became less accurate until 750 Hz; then it again matched the measured. The plots of the measured and calculated FRF are visible in Figure 11. The FRAC numbers from Table 2 confirm the results.

### FRFs Between Right-Front Arm and Top-Strut Mount

The top strut mount connection point is a place where excitation is difficult to perform with the classic method of hammer impact or shaker. The solution for this issue would be to acquire the reciprocal FRFs, or the driving point information will be lost. The only choice remains to use the inertial shaker. This case proves the utility of this type of shaker. By adding the 3D adapter to the setup, it extends its utility by excluding the necessity of excitation in the vehicle axis.

The front-right top strut mount connection and front right arm front connection are noted with FDOM:FRRI, respectively FRAR:FRON. The FRFs between them are shown in Figure 12. The reciprocity matches only up to 160 Hz, and then it gets worse. The calculated reciprocal FRF still fits the measured one, except in the frequency range between 600-800 Hz. This means the main issue comes from the direct transfer function. The FRAC values in Table 3 are low, confirming the bad reciprocity.

### Assumptions of Nonreciprocity

**Interference of Stinger Modes**. When the inertial shaker was attached to the 3D adapter, some irregularities were visible between 500-800 Hz on almost all the calculated FRFs. For this reason, a particular experiment was done to analyze the problem. A stiff metal plate was chosen as a test object. The 3D adapter was glued on top and the shaker was installed to create an angle with the horizontal plane (see Figure 13). The FRFs between the force input and the driving-point response accelerations in X, Y and Z directions were acquired and are shown in Figure 14.

The peaks and dips from the FRFs in Figure 14 were in the same frequency range as the ones from the vehicle FRFs. They could be related to the stinger, and to remove them from the frequency of interest, use of a stiffer stinger was considered beneficial. To check the assumption, the test was repeated with a shorter stinger, and the peaks were shifted above 1000 Hz (see Figure 15).

**Mass and Moment Effects of Support Block.** This particular case reveals the errors encountered when using a rectangular prism support to excite with the shaker in the vehicle axis X or Y at the top-strut mount location (see Figure 16). There are two main disadvantages when using this technique: a mass-loading effect and a torque effect. The mass-loading effect is amplified in this case, because the block is attached to a low-stiffness steel plate and makes the FRF sensitive to local behavior.

*Table 1. FRAC for direct and reciprocal FRFs between front-arm connection points.*

|  | 30 - 300 Hz | 300 - 600 Hz | 600 - 2000 Hz |
|---|---|---|---|
| Measured FRAC | 1 | 0.98 | 0.90 |
| Calculated FRAC | 1 | 0.93 | 0.81 |

*Table 2. FRAC for reciprocal FRFs between front- and rear-arm connection points.*

|  | 30 - 300 Hz | 300 - 600 Hz | 600 - 2000 Hz |
|---|---|---|---|
| Measured FRAC | 1 | 0.98 | 0.92 |
| Calculated FRAC | 1 | 0.97 | 0.81 |

*Table 3. FRAC for reciprocal FRFs between front-front arm and top-strut mount connections.*

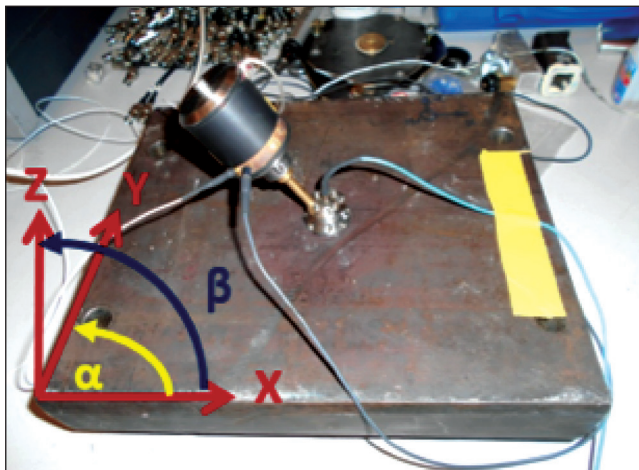|  | 30 - 300 Hz | 300 - 600Hz | 600 - 2000 Hz |
|---|---|---|---|
| Measured FRAC | 0.96 | 0.37 | 0.10 |
| Calculated FRAC | 0.97 | 0.44 | 0.24 |

Figure 13. Setup for studying stinger modes.
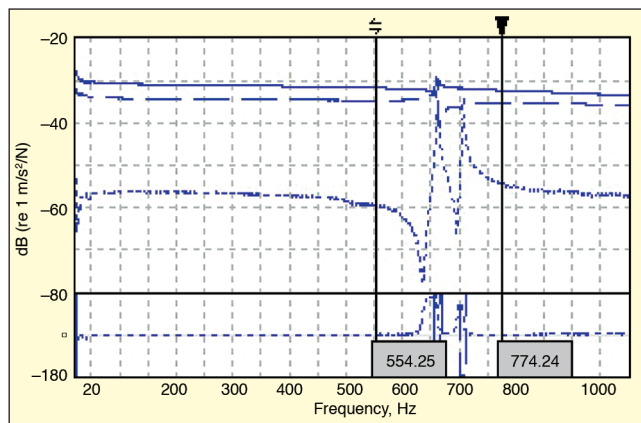


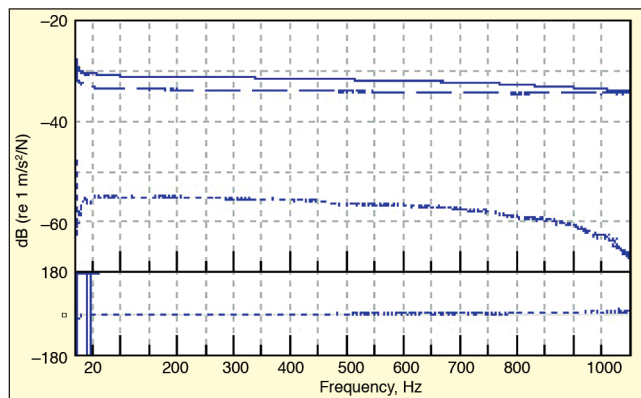Figure 14. Driving-point FRFs with long stinger



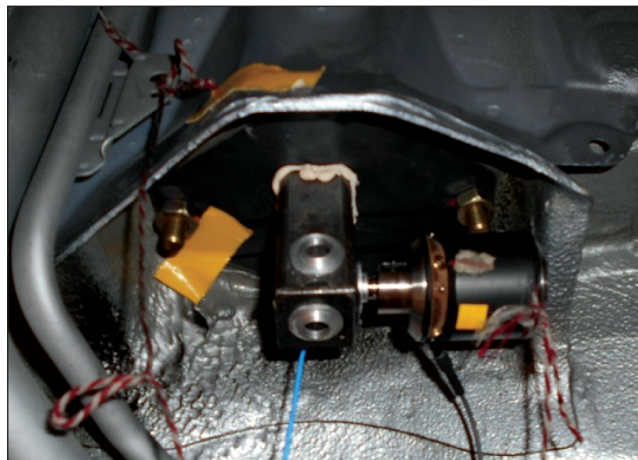Figure 15. Driving point FRFs with short stinger.



Figure 16. LMS Qsources Integral Shaker on steel block at the rear strut mount location.
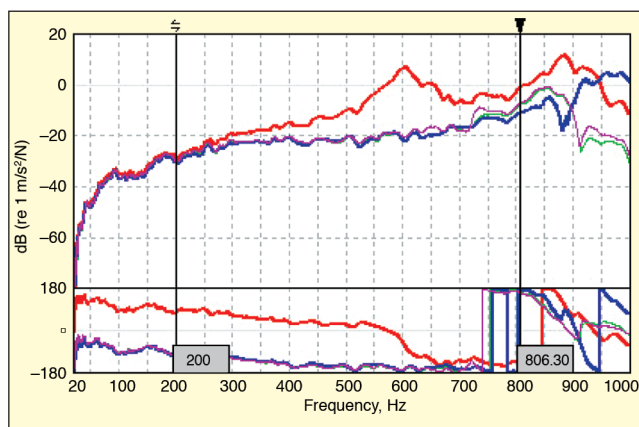


Figure 17. Direct and reciprocal FRFs between the rear-right top-strut mount and the rear arm rear connections: red bold line – direct FRF measured; red dotted line – reciprocal FRF measured; blue bold line – direct FRF calculated; blue dotted line – reciprocal FRF calculated.



Figure 18. Inertia shaker attached to stiff aluminum plate glued to the original top-strut mount.

The advantage of using the 3D adapter becomes evident when the measured and calculated FRFs are compared in Figure 17. The FRFs are taken between the rear top-strut mount RDOM:RERI to the rear arm connection named RSUB:RERI. The calculated direct FRF from the 3D adapter excitation matched the reciprocal FRFs, both measured and calculated, up to a frequency of 800 Hz. The measured one matched the reciprocal only up to a frequency of 200 Hz. From this example it was obvious that by using the 3D adapter, the quality of the FRF would improve toward higher frequency domain.

**Final Modifications of Setup for Improving FRF Acquisition**. By taking in consideration all previous assumptions, the measurements at the front top-strut mount were repeated after the setup was modified. A short stinger was used instead of a longer one. The steel plate was replaced by the original support to which an aluminum stiff plate was glued. The new setup is shown in Figure 18.

The previous FRAC matrices from Figures 8 and 9, showed that there were miss-correlations between the direct and reciprocal

FRFs between the top-strut mount point and the other suspension locations above the frequency of 300 Hz. They were recalculated with the FRFs from the new set of measurements. The FRAC results are shown in Figures 19 and 20 for the measurements and reconstructed FRF respectively. The driving-point FRFs were significantly improved in such a way that the FRAC criterion's value was 1 or close to 1, which means an almost a perfect match. The cross-vehicle FRFs were also improved to obtain high values and good reciprocity.

One of the most important benefits of this method is improving the quality of local structural FRFs. The tri-axial accelerometer is

| | FDOM | FDOM | FDOM | FRAR | FRAR | FRAR |
|---|---|---|---|---|---|---|
| | FRRI:X | FRRI:Y | FRRI:Z | REAR:X | REAR:Y | REAR: |
| FDOM:FRRI:X | 1.00 | 1.00 | 1.00 | 1.00 | 0.99 | 1.00 |
| FDOM:FRRI:Y | 1.00 | 1.00 | 1.00 | 0.97 | 0.98 | 1.00 |
| FDOM:FRRI:Z | 1.00 | 1.00 | 1.00 | 0.87 | 0.98 | 1.00 |
| FRAR:REAR:X | 1.00 | 0.97 | 0.87 | 1.00 | 0.99 | 1.00 |
| FRAR:REAR:Y | 0.99 | 0.98 | 0.98 | 0.99 | 1.00 | 0.92 |
| FRAR:REAR:Z | 1.00 | 1.00 | 1.00 | 1.00 | 0.92 | 1.00 |

Figure 19. Extract from the FRAC matrices of direct and reciprocal FRFs from 30 to 300 Hz (reconstructed FRFs).

| | FDOM | FDOM | FDOM | FRAR | FRAR | FRAR |
|---|---|---|---|---|---|---|
| | FRRI:X | FRRI:Y | FRRI:Z | REAR:X | REAR:Y | REAR: |
| FDOM:FRRI:X | 1.00 | 1.00 | 0.99 | 0.83 | 0.93 | 0.98 |
| FDOM:FRRI:Y | 1.00 | 1.00 | 1.00 | 0.97 | 0.97 | 0.98 |
| FDOM:FRRI:Z | 0.99 | 1.00 | 1.00 | 0.79 | 0.86 | 0.98 |

Figure 20. Extract from the FRAC matrices of direct and reciprocal FRFs from 300 to 600 Hz (reconstructed FRFs).

situated inside the 3D adapter at the intersection of all possible excitation centerlines. The offset between excitation and driving-point accelerometer is removed. The direct and reciprocal FRFs on the front top-strut mount location are plotted in Figure 21

## Discussion

The calculated FRF should not be influenced by the number of over-determination excitation points on the 3D adapter chosen to calculate the orthogonal FRFs. However, when the longer stinger is used, the error due to the stinger modes was amplified when a larger set of excitation points was used for calculation. The results showed an offset to the reference curve in the range of 600-800 Hz. The resonance is the first bending mode of the connection between shaker and 3D adapter. A design update can shift the stinger resonance outside the frequency range of interest.

## Conclusions

The space constraints form an ever-increasing challenge for body NVH testing in the measurement laboratory. The proposed method diminishes several shortcomings of existing methods by:
• Making body connection points accessible.
• Removing the negative effect of moment input caused by local added impact support.
• Enabling user-independent and repeatable results.
• Reducing the effect of mass loading.
• Allowing driving-point accelerometer response at the center of excitation.

The configuration where the inertial shaker is used directly is more efficient. The method proposed here can serve as an addi-
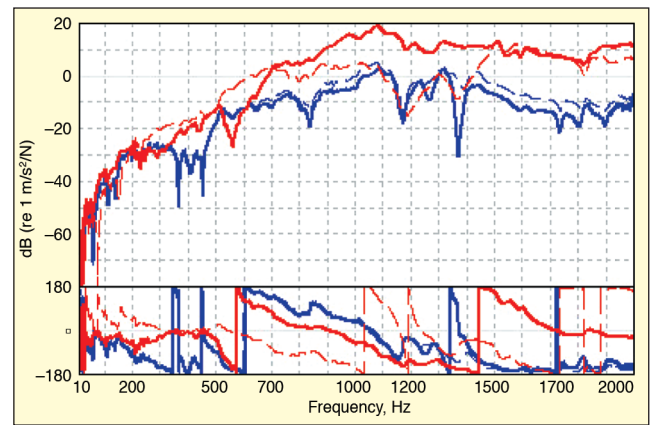


Figure 21. Direct and reciprocal local cross FRFs at excitation location in Y and Z directions: red bold line – direct FRF measured; red dotted line – reciprocal FRF measured; blue bold line – direct FRF calculated; blue dotted line – reciprocal FRF calculated.

tional method next to the use of inertial shakers for error-sensitive locations. This method also shows potential for other NVH methods like CAE correlation and for structural modal analysis, where correct local-driving point information is essential in obtaining accurate modal models. This can be a topic for future work.

## References

1. Florentin, J., Durieux, F., Kuriyama, Y., and Yamamoto, T., "Electric Motor Noise in a Lightweight Steel Vehicle," SAE Technical Paper 2011-01-1724, 2011, DOI:10.4271/2011-01-1724.
2. Wang, A., Liao W. and Hein A., "A Perspective on China's Auto Market in 2020," McKinsey & Co., November 2012.
3. Daves, G., "Automotive Packaging Trends," Semiconwest 2014, July 2014.
4. Van der Auweraer, H., Janssens, K., "A Source-Transfer-Receiver Approach to NVH Engineering of Hybrid/Electric Vehicles," SAE Technical Paper 2012-36-0646, 2012.
5. Johnson, M., Kirchain R. "The Importance of Product Development Cycle Time and Cost in the Development of Product Families," *Journal of Engineering Design*, Vol. 22, Iss. 2, 2011.
6. Geluk, T., Van der Linden, P., "Noise Contribution Analysis at Suspension Interfaces Using Different Force Identification Techniques," SAE Technical Paper 2011-01-1600, May 2011, DOI:10.4271/2011-01-1600.
7. Shin, T., Shin, K., Lee, S., "Development of Road Noise Estimation Technology Based on Character of Tire and Matrix Inversion Method," RASD 2013, Italy, July 2013.
8. Koners, G., Lehmann R., "Investigation of Tire-Road Noise with Respect to Road-Induced Wheel Forces and Radiated Airborne Noise," SAE Technical Paper 2014-01-2075, DOI:10.4271/2014-01-2075, June 2014.
9. Coster, C., Nagahata, D., van der Linden, P. J. G., "On the accuracy Reciprocal and Direct Vibroacoustic Transfer Function Measurements on Vehicles for Lower and Medium Frequencies," ISMA 2010, Paper ID 243, Belgium, September 2010.
10. Chen, Anning, "Frequency Response Assurance Criterion and Applications to Model Correlation of Body Structures," SAE Technical Paper, 2003-01-1737, 2003.
11. Rao, C. R., Mitra, S. K., *Generalized Inverse of Matrices and its Applications*, ISBN: 0471708216 (0-471-70821-6), Wiley, New York, 1971. **S|V**

The author can be reached at: tom.knechten@siemens.com.